Pure Appl. Geophys. 183 (2026), 3433–3451
© 2026 The Author(s), under exclusive licence to Springer Nature Switzerland AG
https://doi.org/10.1007/s00024-026-04012-0

Pure and Applied Geophysics

Simulation of Wave Propagation in Cosserat Micropolar Media

José M. Carcione,[1,5] Mamdoh Alajmi,[2] Ayman N. Qadrouh,[2] Juan E. Santos,[1,3,4] and Jing Ba[1]

Abstract—In the Cosserat micropolar theory, the stress tensor is asymmetric, with the antisymmetric part representing micro rotations, for example, of material particles such as grains in granular porous media. The solution of the differential equations includes the classical P and S waves, as well as two micro-rotation waves, whose effects become significant at high frequencies. Explicit expressions for the phase and group velocities as functions of frequency and wavenumber for a plane wave are derived. In homogeneous media, the P wave is not affected by the micro-rotations, and the S wave is coupled to the micro-rotation waves, it is dispersive and has the same velocity as in the classical theory of elasticity at low frequencies. To our knowledge, there are no simulations of micro-rotation waves as single wavefronts in the literature; only their effects on the particle displacements are simulated. A direct grid method, based on the Fourier pseudospectral method for computing spatial derivatives and a fourth-order Runge–Kutta algorithm for time integration, calculates the wavefield in the space-time domain and simulates micro-rotation wavefronts. A stability analysis verifies the conditions under which the algorithm solves the Cosserat differential equations.

Keywords: Cosserat micropolar theory, micro-rotation waves, Fourier method, Runge–Kutta algorithm, direct grid method.

1. Introduction

Differences between the classical theory of elasticity and experiments arise in porous media at high frequencies when the wavelength is comparable to the average grain size and the rotational motion of the grains is considered. If the phenomenon under study has a characteristic length (such as wavelength) comparable to the size of the grains in the body, then the microstructure of the material becomes important and must be taken into account. The general theory is termed micropolar and is based on the Cosserat theory (Cosserat & Cosserat, 1909). Lakes (1986) identified additional elastic constants in polymeric foams, and Merkel et al. (2011) experimentally detected the propagating rotational-shear mode in granular crystals (beads). Hassanpour and Heppler (2015) in their table 4 provide a set of micropolar constants for some materials, mainly obtained by Lakes and co-workers.

Cosserat and Cosserat (1909) assumed that the body consists of interconnected particles (e.g grains) in the form of small rigid bodies. During deformation, each particle is displaced by the vector $\mathbf{u}$ and rotated by a micro-rotation vector $\boldsymbol{\varphi}$. This results in micro-rotation waves (labelled R here), in addition to the classical P and S waves. Parfitt and Eringen (1966) identify six waves in isotropic media: P and R_1, S_1 and S_2 (referred to as S here) with the same velocity, and R_2 and R_3 with the same velocity (referred to as R_2 here). They show that the S wave is dispersive, the R_1 wave is compressional and the R_2 wave is shear; the latter two are also dispersive and exist only above a cutoff frequency $\omega_0 = 2\sqrt{\alpha/J}$, where α is a micropolar constant and J the rotational-inertia density. Merkel and Luding (2017) describe the interaction of identical beads with a discrete approach, where the displacement and rotation of each individual bead are taken into account. They compare the results with the micropolar theory and suggest a modification of the latter.

To our knowledge, there are no simulations of micro-rotation waves as single wavefronts using Cosserat theory. Sadovskaya & Sadovskii (2012, Eq. 10.7 and Fig. 10.19) identify the four

[1] School of Earth Sciences and Engineering, Hohai University, Nanjing, China. E-mail: jcarcione@ogs.it; jingba@188.com
[2] KACST, PO Box 6086, Riyadh, 11442, Saudi Arabia.
[3] Facultad de Ingeniería, Instituto del Gas y del Petróleo, Universidad de Buenos Aires, Buenos Aires, Argentina.
[4] Department of Mathematics, Purdue University, West Lafayette, USA.
[5] National Institute of Oceanography and Applied Geophysics - OGS, Trieste, Italy.

velocities of the P and S waves, as well as the longitudinal and transverse rotational waves, and the events in a micro-seismogram of Lamb's problem, where the waves are intermixed in a single wave packet. They solve the system of equations using a second-order Crank-Nicolson scheme. Other studies only examine their effects on classical waves at relatively low frequencies, assuming hypothetical micropolar constants (Abreu et al., 2020; Xiu et al., 2020; Dhabu et al., 2021). A completely different algorithm, the discrete element method (DEM), supports the existence of micro-rotation waves, where the medium consists of separate interacting particles. Buklakov et al. (2023) and Dębski (2025) performed such simulations, observing relatively incoherent rotational waves. The former authors found that displacements and coherent rotations of the shear wave move at the same velocity, and that rotations are more significant at high frequencies. These are characteristics of Cosserat media. The DEM algorithm could therefore be used to quantify the micropolar constants.

Here, we consider the theory presented in Nowacki (1974), who extensively develops the complete theory of asymmetric elasticity, which was introduced by the brothers François and Eugéne Cosserat, who published it in 1909 in the work "Théorie des corps déformables". The discussion begins with dynamic problems, then considers the static ones. In particular, the micropolar differential equations can be decomposed into two mutually independent systems of equations, and this is the case we solve here with a numerical algorithm. We first perform a plane-wave analysis, which provides the wave velocities of the P, S, R_1, and R_2 modes. We then solve the governing equations using a fourth-order Runge–Kutta algorithm for time stepping (e.g., Jain, 1984, pp. 71–72; Carcione 2022, Section 9.2.3) and the Fourier pseudospectral method to compute the spatial derivatives (e.g., Carcione 2022, Section 9.3.2), which is infinitely accurate for band-limited periodic functions with cutoff spatial wavenumbers smaller than the cutoff wavenumbers of the mesh. A stability analysis illustrates the conditions under which the numerical solution of the differential equations is stable.

The novelty of our work is that this is the first simulation of micro-rotation waves since their discovery by the Cosserat brothers. The two uncoupled equations from Nowacki (1974) paper have not been solved before. Previous studies do not show these waves, which appear at high frequencies. There are simulations (which we cite), but they do not show the waves explicitly because they were conducted at low frequencies. These micro-rotation waves behave similarly to the slow Biot wave in porous media (e.g., Carcione 2022), as they are propagating waves at high frequencies. However, in this case, there is a cut-off frequency, and Biot waves are diffusive at low frequencies.

2. Equations of Motion

Let us consider an isotropic 3D medium described by the micropolar theory, where the displacement and rotation vectors are

$$\mathbf{u} = (u_1, u_2, u_3) \quad \text{and} \quad \boldsymbol{\varphi} = (\varphi_1, \varphi_2, \varphi_3), \tag{1}$$

respectively. Following Nowacki (1974), the equations of motion are

$$\begin{aligned}
\rho \ddot{u}_i &= \sigma_{ji,j} + X_i, && (2.1)\\
J \ddot{\varphi}_i &= \epsilon_{ijk}\sigma_{jk} + \tau_{ji,j} + Y_i, && (2.1)\\
\sigma_{ji} &= (\mu + \alpha)\gamma_{ji} + (\mu - \alpha)\gamma_{ij} + \lambda \delta_{ij}\gamma_{kk}, && (2.9)\\
\tau_{ji} &= (\gamma + \epsilon)\kappa_{ji} + (\gamma - \epsilon)\kappa_{ij} + \beta \delta_{ij}\kappa_{kk} + T_{ji}, && (2.9)\\
\gamma_{ij} &= u_{j,i} - \epsilon_{ijk}\varphi_k, && (2.5)\\
\kappa_{ij} &= \varphi_{j,i}, && (2.5),
\end{aligned} \tag{2}$$

where

$$
\begin{array}{cc}
u_i : \text{displacement}, & [\text{m}] \\
\varphi_i : \text{rotation}, & \text{unitless} \\
\sigma_{ji} : \text{force stress}, & [\text{Pa: kg/s}^2/\text{m}] \\
\tau_{ji} : \text{moment stress}, & [\text{kg/s}^2] \\
\gamma_{ji} : \text{strain}, & \text{unitless} \\
\kappa_{ji} : \text{twist strain}, & [1/\text{m}] \\
\rho : \text{mass density}, & [\text{kg/m}^3] \\
J : \text{rotational-inertia density}, & [\text{kg/m}] \\
X_i : \text{body force}, & [\text{kg/s}^2/\text{m}^2] \\
Y_i : \text{body moment}, & [\text{kg/s}^2/\text{m}] \\
T_{ji} : \text{moment source}, & [\text{kg/s}^2] \\
\mu, \lambda : \text{Lamé constants}, & [\text{Pa: kg/s}^2/\text{m}] \\
\alpha : \text{micropolar constant}, & [\text{Pa: kg/s}^2/\text{m}] \\
\beta, \epsilon, \gamma : \text{micropolar constants}, & [\text{N: kg m/s}^2] \\
\delta_{ij} : \text{Kronecker delta}, & \text{unitless} \\
\epsilon_{ijk} : \text{Levi-Civita tensor} & \text{unitless},
\end{array}
\tag{3}
$$

where we have indicated the units in the MKS system (J is inertia per unit volume). The numbers in Eq. (2) correspond to the equations in Nowacki (1974). The constants satisfy

$$
\begin{array}{c}
3\lambda + 2\mu > 0, \quad \mu > 0, \quad 3\beta + 2\gamma > 0, \quad \gamma > 0, \\
\mu + \alpha > 0, \quad \gamma + \epsilon > 0, \quad \alpha > 0, \quad \epsilon > 0
\end{array}
\tag{4}
$$

resulting from the fact that the internal energy is a quadratic definite form (Nowacki, 1974, p. 7, Eq. 2.8).

In homogeneous media and in the absence of sources, the equations of motion become

$$
\begin{aligned}
(\mu + \alpha)\nabla^2 \mathbf{u} + (\lambda + \mu - \alpha)\text{grad div } \mathbf{u} + 2\alpha \text{ rot}\boldsymbol{\varphi} &= \rho \ddot{\mathbf{u}}, \\
(\gamma + \epsilon)\nabla^2 \boldsymbol{\varphi} + (\gamma + \beta - \epsilon)\text{grad div } \boldsymbol{\varphi} - 4\alpha\boldsymbol{\varphi} + 2\alpha \text{ rot}\mathbf{u} &= J\ddot{\boldsymbol{\varphi}},
\end{aligned}
\tag{5}
$$

(Nowacki, 1974, Eq. 2.10). Green's functions are given in Nowacki and Nowacki (1969).

There are especial cases of the Cosserat theory. The theory of asymmetric stress given in Qiu (2020) and Carcione et al. (2025) is a particular case of the micropolar equations, where $\beta = \epsilon = \gamma = 0$, $\mu + \alpha = \mu_1$, $\mu - \alpha = \mu_2$, and $2\mu = \mu_1 + \mu_2$.

On the other hand, if $\alpha, \beta \to \infty$, then $\boldsymbol{\varphi} = \frac{1}{2}\nabla \times \mathbf{u}$, and the couple-stress theory is obtained, describing only macro-rotations, or micro-rotations are equivalent to macro-rotations (Hassanpour & Heppler, 2014). Hadjesfandiari and Dargush (2011) solved an indeterminacy of the original couple-stress theory.

If $\alpha = 0$, we obtain from (5) two independent equations, namely, the classical wave equation and that of a hypothetical elastic medium where only micro-rotation wave are possible.

The so-called characteristic length of micro-rotation is of the order of the micro-structure (e.g., grain size, pore radius, etc). It is given by $L_r = \sqrt{\gamma/\mu}$ in Nowacki's notation (Lakes, 1986, p. 59). Lakes (1986) uses Eringen's (E) notation and the equivalence is $\lambda_E = \lambda$, $\mu_E = \mu - \alpha$, $\beta_E = \gamma - \epsilon$, $\gamma_E = \gamma + \epsilon$, $\kappa_E = 2\alpha$ and $\alpha_E = \beta$ (Pujol, 2009, Eq. 120; Hassanpour & Heppler, 2015, Table 3). The constitutive equations in Eringen's notation are

$$
\begin{aligned}
\sigma_{ji} &= \lambda_E \epsilon_{kk}\delta_{ji} + (2\mu_E + \kappa_E)\epsilon_{ji} + \kappa_E \epsilon_{jim}(r_m - \varphi_m), \\
\tau_{ji} &= \alpha_E \varphi_{k,k}\delta_{ji} + \beta_E \varphi_{j,i} + \gamma_E \varphi_{i,j}, \\
r_m &= \tfrac{1}{2}\epsilon_{mln} u_{n,l} \quad \left(\tfrac{1}{2}\nabla \times \mathbf{u}\right)
\end{aligned}
\tag{6}
$$

(Parfitt & Eringen, 1966, Eqs. 1.4 and 1.5; Pujol, 2009, Eqs. 119 and 118), where $\epsilon_{ij} = (1/2)(u_{i,j} + u_{j,i})$. In terms of the Nowacki constants, we have

$$
\begin{aligned}
\sigma_{ji} &= \lambda \epsilon_{kk}\delta_{ji} + 2\mu\epsilon_{ji} + 2\alpha\epsilon_{jim}(r_m - \varphi_m), \\
\tau_{ji} &= \beta \varphi_{k,k}\delta_{ji} + (\gamma - \epsilon)\varphi_{j,i} + (\gamma + \epsilon)\varphi_{i,j}.
\end{aligned}
\tag{7}
$$

Nowacki (1974, p. 13) consider two-dimensional problems. Let us assume a 2D problem in which the displacements are independent of z, such that differentiation along the z-direction vanishes. In such a case, Eq. (2) can be broken down into two independent systems of equations.

2.1. First System of Differential Equations

The following vectors appear in the first system of equations:

$$
\begin{array}{ll}
\mathbf{u} = (u_1, u_2, 0), & \boldsymbol{\varphi} = (0, 0, \varphi_3), \\
\mathbf{X} = (X_1, X_2, 0), & \mathbf{Y} = (0, 0, Y_3),
\end{array}
\tag{8}
$$

Define the particle velocity and rate of rotation as

$$\mathbf{v} = (v_1 = \dot{u}_1, v_2 = \dot{u}_2, 0) \quad \text{and} \quad \boldsymbol{\eta} = (0, 0, \eta = \dot{\varphi}_3), \tag{9}$$

respectively. Now the system of Eq. (2) takes the form

$$\begin{aligned}
\dot{v}_1 &= (\sigma_{11,1} + \sigma_{21,2} + X_1)/\rho,\\
\dot{v}_2 &= (\sigma_{12,1} + \sigma_{22,2} + X_2)/\rho,\\
\dot{\eta} &= (\sigma_{12} - \sigma_{21} + \tau_{13,1} + \tau_{23,2} + Y_3)/J,\\
\dot{\sigma}_{11} &= (\lambda + 2\mu)v_{1,1} + \lambda v_{2,2},\\
\dot{\sigma}_{22} &= (\lambda + 2\mu)v_{2,2} + \lambda v_{1,1},\\
\dot{\sigma}_{12} &= (\mu + \alpha)v_{2,1} + (\mu - \alpha)v_{1,2} - 2\alpha\eta,\\
\dot{\sigma}_{21} &= (\mu + \alpha)v_{1,2} + (\mu - \alpha)v_{2,1} + 2\alpha\eta,\\
\dot{\tau}_{13} &= (\gamma + \epsilon)\eta_{,1},\\
\dot{\tau}_{23} &= (\gamma + \epsilon)\eta_{,2}.
\end{aligned} \tag{10}$$

Equation (10) are the velocity-stress formulation, corresponding to equations 2.21 and 2.22 in Nowacki (1974). While these equations are only valid for homogeneous media and are not suitable for the simulation of wave fields in heterogeneous media using direct methods (finite differences, pseudospectral method, etc.), Eq. (10) are valid in general. Note the constant β is not present in the equations. If $\alpha = \gamma = \epsilon = 0$, the equations of classical elasticity are obtained since $\sigma_{12} = \sigma_{21}$ and $\tau_{13} = \tau_{23} = 0$.

2.2. Second System of Differential Equations

In the second system

$$\mathbf{v} = (0, 0, v_3 = \dot{u}_3) \quad \text{and} \quad \boldsymbol{\eta} = (\eta_1 = \dot{\varphi}_1, \eta_2 = \dot{\varphi}_2, 0), \tag{11}$$

and equations (2) takes the form

$$\begin{aligned}
\dot{v}_3 &= (\sigma_{13,1} + \sigma_{23,2} + X_3)/\rho,\\
\dot{\eta}_1 &= (\sigma_{23} - \sigma_{32} + \tau_{11,1} + \tau_{21,2} + Y_1)/J,\\
\dot{\eta}_2 &= (\sigma_{31} - \sigma_{13} + \tau_{12,1} + \tau_{22,2} + Y_2)/J,\\
\dot{\sigma}_{13} &= (\mu + \alpha)v_{3,1} + 2\alpha\eta_2,\\
\dot{\sigma}_{31} &= (\mu - \alpha)v_{3,1} - 2\alpha\eta_2,\\
\dot{\sigma}_{23} &= (\mu + \alpha)v_{3,2} - 2\alpha\eta_1,\\
\dot{\sigma}_{32} &= (\mu - \alpha)v_{3,2} + 2\alpha\eta_1,\\
\dot{\tau}_{11} &= (2\gamma + \beta)\eta_{1,1} + \beta\eta_{2,2},\\
\dot{\tau}_{22} &= (2\gamma + \beta)\eta_{2,2} + \beta\eta_{1,1},\\
\dot{\tau}_{12} &= (\gamma + \epsilon)\eta_{2,1} + (\gamma - \epsilon)\eta_{1,2} + T_{12},\\
\dot{\tau}_{21} &= (\gamma + \epsilon)\eta_{1,2} + (\gamma - \epsilon)\eta_{2,1} + T_{21}.
\end{aligned} \tag{12}$$

Equations (12) are the velocity-stress formulation, corresponding to equations 2.24 and 2.25 in Nowacki (1974).

3. Plane-Wave Analysis

A plane-wave analysis yields the expression for the velocities and attenuations of the different wave modes. A general plane-wave kernel is

$$\exp[\mathrm{i}(\omega t - \mathbf{k}\cdot\mathbf{x})] = \exp[\mathrm{i}(\omega t - k_1 x_1 - k_2 x_2)], \tag{13}$$

where ω is the angular frequency, $\mathbf{k} = (k_1, k_2)$ is the wavenumber, $\mathbf{x} = (x_1, x_2)$ is the position vector and $\mathrm{i} = \sqrt{-1}$. ω and k can be complex and real, respectively (stationary waves) or real and complex (traveling waves).

In the absence of external forces ($X = Y = T = 0$), we consider plane waves propagating along the (l_1, l_2) direction, where l_1 and l_2 are the direction cosines. We assume homogeneous waves (Carcione, 2022, Eq. 3.27) for which

$$\mathbf{k} = (k_1, k_2) = (l_1, l_2)k, \tag{14}$$

where $k = \sqrt{k_1^2 + k_2^2}$ is the complex magnitude of the wavevector, and $l_1^2 + l_2^2 = 1$. The spatial and time derivatives can be replaced by

$$\partial_1 \to -\mathrm{i}k_1 = -\mathrm{i}kl_1, \quad \partial_2 \to -\mathrm{i}k_2 = -\mathrm{i}kl_2, \quad \partial_t \to \mathrm{i}\omega. \tag{15}$$

3.1. System1.P, Sandblank; R_2 Waves

Consider the first system of Eq. (10). First, we assume that the wavenumber k a real quantity. Using the relations (15) and replacing the stresses into the first three Eq. (10), we obtain an eigenvalue equation

$$(\mathbf{A} - \omega^2\mathbf{I}_3)\cdot\mathbf{w} = 0, \quad \mathbf{w} = (u_1, u_2, \varphi_3)^\top, \tag{16}$$

where

$$\mathbf{A} = \begin{pmatrix} k^2\rho'[El_1^2 + (\mu+\alpha)l_2^2] & k^2\rho' l_1 l_2(\lambda+\mu-\alpha) & -2\mathrm{i}\alpha k\rho' l_2 \\ k^2\rho' l_1 l_2(\lambda+\mu-\alpha) & k^2\rho'[El_2^2 + (\mu+\alpha)l_1^2] & +2\mathrm{i}\alpha k\rho' l_1 \\ +2\mathrm{i}\alpha k J' l_2 & -2\mathrm{i}\alpha k J' l_1 & [(\gamma+\epsilon)k^2 + 4\alpha]J' \end{pmatrix}, \tag{17}$$

to be solved for the three roots ω^2, where $\rho' = 1/\rho$

and $J' = 1/J$. Since the medium is isotropic, it is enough to solve the equation in one direction, say the x-direction. Then $l_1 = 1$, $l_2 = 0$ and

$$\mathbf{A} = \begin{pmatrix} k^2\rho' E & 0 & 0 \\ 0 & k^2\rho'(\mu+\alpha) & 2\mathrm{i}\alpha k\rho' \\ 0 & -2\mathrm{i}\alpha k J' & [(\gamma+\epsilon)k^2 + 4\alpha]J' \end{pmatrix}. \tag{18}$$

An eigenvalue is $\omega^2 = k^2\rho' E$ (11-component) and corresponds to the P wave, and if $\alpha = \gamma = \epsilon = 0$, the classical S-wave can also be obtained (22-component), so the velocities are

$$v_{\mathrm{P}} = \sqrt{E\rho'} = \sqrt{\frac{\lambda+2\mu}{\rho}}, \quad v_{\mathrm{S}} = \sqrt{\frac{\mu}{\rho}}. \tag{19}$$

In the micropolar case, the dispersion equation is obtained by setting the determinant in Eq. (16) equal to zero. From this equation and (18), we obtain

$$\begin{aligned} &[k^2\rho'(\mu+\alpha) - \omega^2]\{[(\gamma+\epsilon)k^2 + 4\alpha]J' - \omega^2\} \\ &- 4\alpha^2 k^2 \rho' J' = 0. \end{aligned} \tag{20}$$

or

$$\begin{aligned} \omega^4 + \mathcal{B}\omega^2 + \mathcal{C} &= 0, \\ \mathcal{B} &= -[\rho'(\mu+\alpha) + J'(\gamma+\epsilon)]k^2 - 4\alpha J', \\ \mathcal{C} &= \rho' J' k^2[(\mu+\alpha)(\gamma+\epsilon)k^2 + 4\mu\alpha], \end{aligned} \tag{21}$$

whose solution is

$$\omega_{1,2} = \sqrt{(-\mathcal{B} \pm \sqrt{\mathcal{B}^2 - 4\mathcal{C}})/2}. \tag{22}$$

If $k = 0$ the solutions are 0, and $2\sqrt{\alpha J'}$. In general, the corresponding phase velocities are

$$v_p = \frac{\mathrm{Re}(\omega)}{k} \tag{23}$$

(Carcione, 2022, Eq. 2.149). The two roots correspond to the S and R_2 waves. The velocity of the energy can be approximated by the group velocity:

$$v_g = \frac{\partial \mathrm{Re}(\omega)}{\partial k} = \mathrm{Re}\left(\frac{\partial \omega}{\partial k}\right) \tag{24}$$

(Carcione, 2022, Eq. 2.89). An explicit calculation of the group velocity from Eq. (22) gives

$$v_g(k) = \frac{1}{4}\mathrm{Re}\left\{\frac{1}{\omega}\left[-\mathcal{B}' \pm \frac{1}{\sqrt{\mathcal{B}^2 - 4\mathcal{C}}}(\mathcal{B}\mathcal{B}' - 2\mathcal{C}')\right]\right\}, \tag{25}$$

where

$$\begin{aligned} \frac{\partial \mathcal{B}}{\partial k} &= \mathcal{B}' = -2k[\rho'(\mu+\alpha) + J'(\gamma+\epsilon)], \\ \frac{\partial \mathcal{C}}{\partial k} &= \mathcal{C}' = 4\rho' J' k[(\mu+\alpha)(\gamma+\epsilon)k^2 + 2\mu\alpha]. \end{aligned} \tag{26}$$

Now, we consider $k = \kappa - \mathrm{i}\bar{\alpha}$ complex (Carcione, 2022, Eq. 2.84) and ω real, where κ is the real wavenumber and $\bar{\alpha}$ is the attenuation factor. Equation (20) can be written as

$$k^4 + Bk^2 + C = 0, \tag{27}$$

where

$$\begin{aligned} B &= \frac{4\rho' J'\mu\alpha - \omega^2[(\mu+\alpha)\rho' + (\gamma+\epsilon)J']}{(\mu+\alpha)(\gamma+\epsilon)\rho' J'}, \\ C &= \frac{\omega^2(\omega^2 - 4\alpha J')}{(\mu+\alpha)(\gamma+\epsilon)\rho' J'}. \end{aligned} \tag{28}$$

whose solution is

$$k_{1,2} = \sqrt{(-B \pm \sqrt{B^2 - 4C})/2)}. \tag{29}$$

Then, we define the phase velocity

$$v_p = \frac{\omega}{\mathrm{Re}(k)} = \frac{\omega}{\kappa} \tag{30}$$

(Carcione, 2022, Eq. 2.86) and attenuation factor

$$\bar{\alpha} = -\mathrm{Im}(k) \tag{31}$$

(Carcione, 2022, Eq. 2.88), respectively.

In this case, the group velocity is

$$v_g(\omega) = \frac{\partial \omega}{\partial \kappa} = \left[\mathrm{Re}\left(\frac{\partial k}{\partial \omega}\right)\right]^{-1} \tag{32}$$

An explicit calculation from Eq. (27) gives

$$\frac{\partial k}{\partial \omega} = \frac{1}{4k}\left[-B' \pm \frac{1}{\sqrt{B^2 - 4C}}(BB' - 2C')\right]. \tag{33}$$

where

$$\frac{\partial B}{\partial \omega} = B' = -\frac{2\omega[(\mu+\alpha)\rho' + (\gamma+\epsilon)J']}{(\mu+\alpha)(\gamma+\epsilon)\rho' J'},$$
$$\frac{\partial C}{\partial \omega} = C' = \frac{4\omega(\omega^2 - 2\alpha J')}{(\mu+\alpha)(\gamma+\epsilon)\rho' J'}. \tag{34}$$

Another approach to obtain the phase velocity and attenuation factor as a function of frequency is based on the complex velocity

$$v = \sqrt{\frac{\omega}{k}}. \tag{35}$$

Dividing (20) by k^4, we obtain

$$[\rho'(\mu+\alpha) - v^2]\left[(\gamma+\epsilon)J' + (\Omega-1)v^2\right] - \alpha\rho'\Omega v^2 = 0. \tag{36}$$

where

$$\Omega = \frac{4\alpha J'}{\omega^2}. \tag{37}$$

After some calculations, Eq. (36) can be written as

$$v^4 + Bv^2 + C = 0, \tag{38}$$

where

$$B = [(\gamma+\epsilon)J' + \alpha\rho'\Omega]/(\Omega-1) - (\mu+\alpha)\rho',$$
$$C = -(\mu+\alpha)(\gamma+\epsilon)\rho' J'/(\Omega-1), \tag{39}$$

whose solution is

$$v_{1,2} = \sqrt{(-B \pm \sqrt{B^2 - 4C})/2)}. \tag{40}$$

Then, we obtain the phase velocity

$$v_p = \left[\mathrm{Re}\left(\frac{1}{v}\right)\right]^{-1} \tag{41}$$

and attenuation factor

$$\bar{\alpha} = -\omega \mathrm{Im}\left(\frac{1}{v}\right), \tag{42}$$

respectively, as above.

In this case, the group velocity is

$$v_g(\omega) = \frac{\partial \omega}{\partial \kappa} = \left[\mathrm{Re}\left(\frac{\partial k}{\partial \omega}\right)\right]^{-1} = \left[\mathrm{Re}\left(\frac{\partial(\omega/v)}{\partial \omega}\right)\right]^{-1}$$
$$= \left\{\mathrm{Re}\left[\frac{1}{v}\left(1 - \frac{\omega}{v}\frac{\partial v}{\partial \omega}\right)\right]\right\}^{-1}. \tag{43}$$

3.2. *System2.S, R_2andblank; R_1Waves*

Consider the second system of Eq. (12). Using the relations (15) and replacing the stresses into the first three Eq. (12), we obtain an eigenvalue equation similar to (16) with $\mathbf{w} = (u_3, \varphi_1, \varphi_2)^\top$. Since the medium is isotropic, we assume only for this derivation that $l_1 = 1$ and $l_2 = 0$, and obtain

$$\det \begin{pmatrix} \rho'(\mu+\alpha)k^2 - \omega^2 & 0 & 2\mathrm{i}\alpha k\rho' \\ 0 & [(2\gamma+\beta)k^2 + 4\alpha]J' - \omega^2 & 0 \\ -2\mathrm{i}\alpha k J' & 0 & J'[4\alpha + (\gamma+\epsilon)k^2] - \omega^2 \end{pmatrix} = 0. \tag{44}$$

An eigenvalue is $\omega^2 = [(2\gamma+\beta)k^2 + 4\alpha]J'$ (22-component) and corresponds to a compressional or longitudinal micro-rotation wave R_1 (Parfitt & Eringen, 1966, Eq. 1.31; Nowacki, 1974, Eqs. 2.14 and 2.29). The phase velocities, given by ω/k, are

$$v_{p\mathrm{R}_1}(k) = \sqrt{\frac{1}{J}\left[(2\gamma+\beta)+\frac{4\alpha}{k^2}\right]}, \quad \text{and}$$
$$v_{p\mathrm{R}_1}(\omega) = \sqrt{\frac{2\gamma+\beta}{J-4\alpha/\omega^2}}. \tag{45}$$

If $\omega = 2\sqrt{\alpha/J} = \omega_0$ the wave has infinite velocity and below this frequency does not exist. Moreover, the determinant in Eq. (44) gives the dispersion Eq. (20), with an additional micro-rotation wave R_2 and the S wave, whose properties were analyzed above. The same cutoff frequency ω_0 applies to the R_2 wave.

The attenuation factor of the R_1 wave is given by Eq. (31) and we obtain

$$\bar{\alpha} = -\mathrm{Im}\sqrt{\frac{(\omega^2-\omega_0^2)J}{2\gamma+\beta}} = -\sqrt{\frac{(\omega_0^2-\omega^2)J}{2\gamma+\beta}}, \quad \omega<\omega_0, \tag{46}$$

and $\bar{\alpha} = 0$ if $\omega \geq \omega_0$.

The group velocities of the R_1 wave, given by $\partial\omega/\partial k$, are

$$v_{g\mathrm{R}_1}(k) = \frac{2\gamma+\beta}{Jv_{p\mathrm{R}_1}(k)}, \quad \text{and} \quad v_{g\mathrm{R}_1}(\omega) = \frac{2\gamma+\beta}{Jv_{p\mathrm{R}_1}(\omega)}, \tag{47}$$

showing that they are reciprocals of the phase velocities.

4. Numerical Solution

Equations (10) can be written in matrix form as

$$\dot{\mathbf{w}} = \mathbf{M}\,\mathbf{w} + \mathbf{s},$$
$$\mathbf{w} = (v_1, v_2, \eta, \sigma_{11}, \sigma_{22}, \sigma_{12}, \sigma_{21}, \tau_{13}, \tau_{23})^\top, \tag{48}$$
$$\mathbf{s} = (X_1/\rho, X_2/\rho, Y_3/J, 0, 0, 0, 0, 0, 0)^\top,$$

where

where $\rho' = 1/\rho$, $J' = 1/J$ and $E = \lambda + 2\mu$.

$$\mathbf{M} = \begin{pmatrix} 0 & 0 & 0 & \rho'\partial_1 & 0 & 0 & \rho'\partial_2 & 0 & 0 \\ 0 & 0 & 0 & 0 & \rho'\partial_2 & \rho'\partial_1 & 0 & 0 & 0 \\ 0 & 0 & 0 & 0 & 0 & J' & -J' & J'\partial_1 & J'\partial_2 \\ E\partial_1 & \lambda\partial_2 & 0 & 0 & 0 & 0 & 0 & 0 & 0 \\ \lambda\partial_1 & E\partial_2 & 0 & 0 & 0 & 0 & 0 & 0 & 0 \\ (\mu-\alpha)\partial_2 & (\mu+\alpha)\partial_1 & -2\alpha & 0 & 0 & 0 & 0 & 0 & 0 \\ (\mu+\alpha)\partial_2 & (\mu-\alpha)\partial_1 & +2\alpha & 0 & 0 & 0 & 0 & 0 & 0 \\ 0 & 0 & (\gamma+\epsilon)\partial_1 & 0 & 0 & 0 & 0 & 0 & 0 \\ 0 & 0 & (\gamma+\epsilon)\partial_2 & 0 & 0 & 0 & 0 & 0 & 0 \end{pmatrix}, \tag{49}$$

On the other hand, Eq. (12) can be written in matrix form as

$$\dot{\mathbf{w}} = \mathbf{M}\ \mathbf{w} + \mathbf{s},$$
$$\mathbf{w} = (v_3, \eta_1, \eta_2, \sigma_{13}, \sigma_{31}, \sigma_{23}, \sigma_{32}, \tau_{11}, \tau_{22}, \tau_{12}, \tau_{21})^\top,$$
$$\mathbf{s} = (X_3/\rho, Y_1/J, Y_2/J, 0, 0, 0, 0, 0, 0, T_{12}, T_{21})^\top, \tag{50}$$

where

The equations are solved with a 4th-order Runge Kutta algorithm, discretizing the time variable as $t = ndt$, where dt is the time step (e.g. Carcione, 2022, Section 9.2.3). The field vector at $(n+1)dt$ is

$$\mathbf{w}^{n+1} = \mathbf{w}^n + \frac{dt}{6}(\Delta_1 + 2\Delta_2 + 2\Delta_3 + \Delta_4), \tag{52}$$

where

$$\Delta_1 = \mathbf{M}\ \mathbf{w}^n + \mathbf{s}^n,$$
$$\Delta_2 = \mathbf{M}\left(\mathbf{w}^n + \frac{dt}{2}\Delta_1\right) + \mathbf{s}^{n+1/2},$$
$$\Delta_3 = \mathbf{M}\left(\mathbf{w}^n + \frac{dt}{2}\Delta_2\right) + \mathbf{s}^{n+1/2},$$
$$\Delta_4 = \mathbf{M}\ (\mathbf{w}^n + dt\Delta_3) + \mathbf{s}^{n+1}.$$

The model is discretized on a regular mesh and the spatial derivatives are calculated with the Fourier method by using the Fast Fourier Transform (Carcione, 2022, Section 9.3.2). This approach is called "pseudospectral" and it is infinitely accurate for band-limited periodic functions with cutoff spatial wavenumbers smaller than the cutoff wavenumbers of the mesh. The conditions are maximum frequency $f_{\max} = v_{\min}/(2dx_{\max})$ and $dt < (2/\pi)dx_{\min}/v_{\max}$, where f, dx and v denote source frequency, grid spacing and wave velocity (Carcione, 2022, Section 9.7).

$$\mathbf{M} = \begin{pmatrix}
0 & 0 & 0 & \rho'\partial_1 & 0 & \rho'\partial_2 & 0 & 0 & 0 & 0 & 0 \\
0 & 0 & 0 & 0 & 0 & J' & -J' & J'\partial_1 & 0 & 0 & J'\partial_2 \\
0 & 0 & 0 & -J' & J' & 0 & 0 & 0 & J'\partial_2 & J'\partial_1 & 0 \\
(\mu+\alpha)\partial_1 & 0 & 2\alpha & 0 & 0 & 0 & 0 & 0 & 0 & 0 & 0 \\
(\mu-\alpha)\partial_1 & 0 & -2\alpha & 0 & 0 & 0 & 0 & 0 & 0 & 0 & 0 \\
(\mu+\alpha)\partial_2 & -2\alpha & 0 & 0 & 0 & 0 & 0 & 0 & 0 & 0 & 0 \\
(\mu-\alpha)\partial_2 & 2\alpha & 0 & 0 & 0 & 0 & 0 & 0 & 0 & 0 & 0 \\
0 & (2\gamma+\beta)\partial_1 & \beta\partial_2 & 0 & 0 & 0 & 0 & 0 & 0 & 0 & 0 \\
0 & \beta\partial_1 & (2\gamma+\beta)\partial_2 & 0 & 0 & 0 & 0 & 0 & 0 & 0 & 0 \\
0 & (\gamma-\epsilon)\partial_2 & (\gamma+\epsilon)\partial_1 & 0 & 0 & 0 & 0 & 0 & 0 & 0 & 0 \\
0 & (\gamma+\epsilon)\partial_2 & (\gamma-\epsilon)\partial_1 & 0 & 0 & 0 & 0 & 0 & 0 & 0 & 0
\end{pmatrix}. \tag{51}$$

5. Examples

Let us consider the example in Section 7.3 of Sluys (1992). The data reported in Section 7.4.1 are v = 0.4 (Poisson ratio) $\lambda = 2v\mu/(1-2v)$, l = 5 mm, with $J = 2\rho l^2/(1+v)$. Comparing Eqs. 7.25 and 7.26 in Sluys (1992) with the 2nd and 3rd Eqs. 2.21 in Nowacki (1974), the equivalence is $u_y = u_2$, $\omega_z = \varphi_3$, $\mu_c = \alpha$, $\Theta = J$ and $2\mu l^2 = \gamma + \epsilon$. These data gives a P-wave velocity of 6387 m/s, and the

Table 1

Medium properties (Sluys, 1992)

λ	13.6 GPa
μ	3.4 GPa
α	1 GPa
β	8.5 kN
ϵ	153 kN
γ	17 kN
ρ	500 kg/m^3
J	0.018 kg/m

values listed in Table 1. Figure 1 shows the frequency and phase velocities of the R_2 and S waves as a function of the wavenumber, corresponding to Eqs. (22) and (23). There is a cutoff frequency $\sqrt{\alpha/J}/\pi$ = 75.3 kHz for the R_2 wave. The group velocity (24) as a function of the wavenumber is shown in Fig. 2.

Figure 3 shows the phase velocity (41) (**a**) and attenuation factor (42) as a function frequency. The plots show that the S wave is dispersive but exhibits no attenuation as a function of frequency.

This behaviour, apparently in contrast to the Kramers-Kronig relations and causality (Carcione, 2022, Section 2.3.2), has not been studied in the literature and deserves a detailed investigation, but as a reviewer noticed, "the Kramers-Kronig relations strictly enforce the pairing of dispersion and attenuation in systems featuring dissipative energy loss (like friction or viscosity). The S wave in the Cosserat model experiences "structural dispersion" due to a purely mechanical, lossless coupling with grain rotations. Having a frequency-dependent velocity without energy dissipation is physically sound, entirely expected in structured media, and, to my knowledge, does not violate causality".

On the other hand, the R_2 wave is strongly attenuated till the cut-off frequency. The group velocity is displayed in Fig. 4. On the other hand, the phase and group velocities (45) and (47) for the R_1 wave are shown in Fig. 5. It can be seen that at the cut-off frequency the phase velocity of the R_1 wave tends to infinity.

To obtain these curves, we have assumed $\gamma = \epsilon/9$ and $\beta = \gamma/2$ (see Table 1). In this case, the characteristic length is L_r = 2.24 mm. The attenuation factor (46) of the R_1 wave as a function frequency is shown

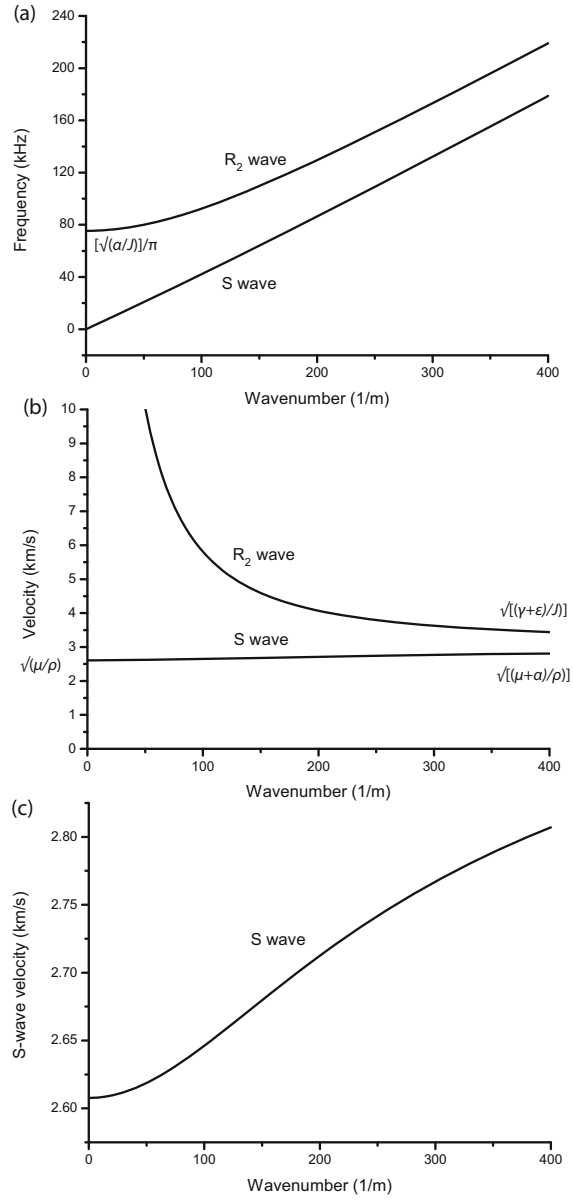


Figure 1
Frequency, $\omega/(2\pi)$ (**a**), and velocities, ω/k, (**b** and **c**) as functions of wavenumber. Figure 1c is a zoomed plot to better show the S-wave velocity dispersion

in Fig. 6. Beyond the cutoff frequency ω_0 there is no attenuation. Summarizing, the group velocities of all the modes are shown in Fig. 7, indicating the values at the low and high frequency limits.

Consider now the numerical solution of the wave Eqs. (48–49). Let us assume a vertical force X_2 whose time history is

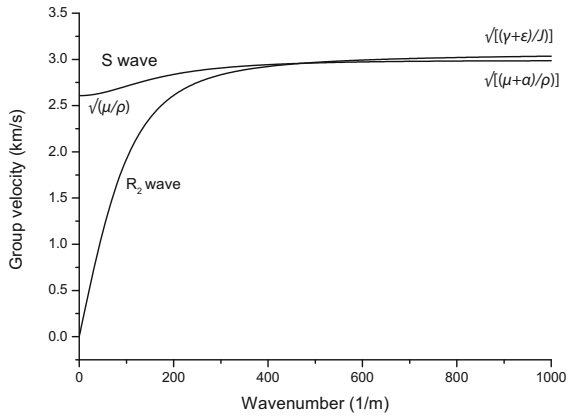


Figure 2
Group velocity (24) as a function of the wavenumber

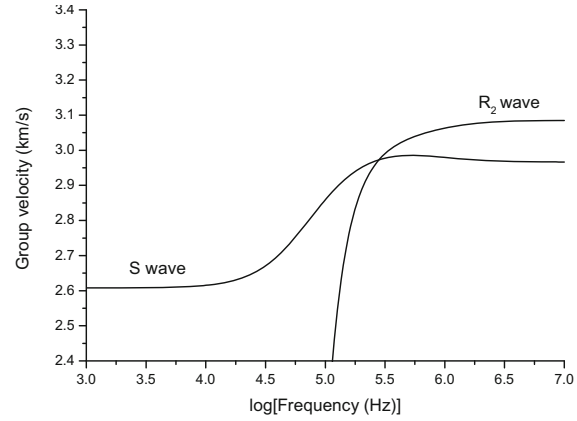


Figure 4
Group velocity (32) as a function of frequency

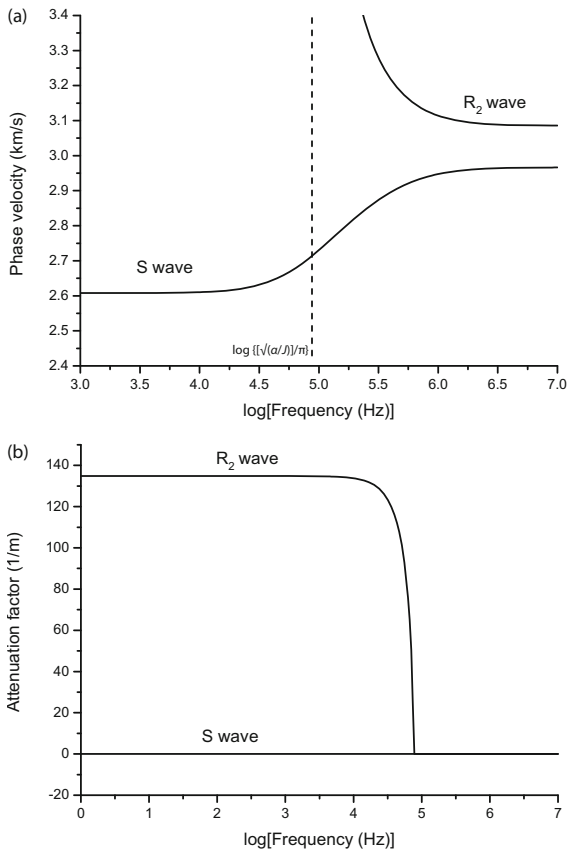


Figure 3
Phase velocity (41) (**a**) and attenuation factor (42) as a function frequency

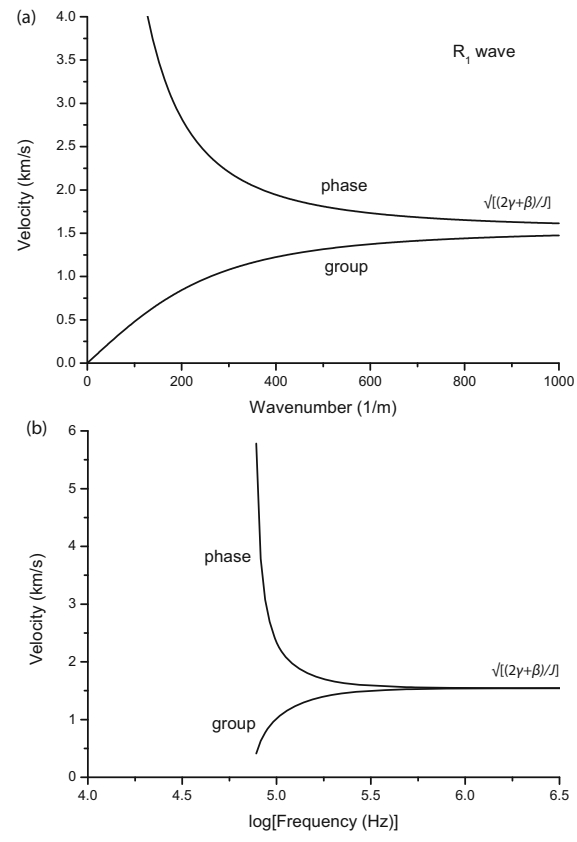


Figure 5
Phase and group velocities (45) and (47) as a function of the wavenumber (**a**) and frequency (**b**)

$$h(t) = \left(o - \frac{1}{2}\right)\exp(-o), \quad o = \left[\frac{\pi(t - t_s)}{t_p}\right]^2, \tag{53}$$

where t_p is the period of the wave and we take $t_s = 1.4t_p$. The peak frequency is $f_p = 1/t_p$.

In the first simulation, the numerical mesh has uniform vertical and horizontal grid spacings of $dx = dy = 10$ m, and 231×231 grid points. The vertical force ($X_2 = 1$) is applied at the center of the mesh with a peak frequency $f_p = 20$ Hz. According to the stability analysis of Appendix A, the eigenvalues of matrix **M** for the first system of equations are shown in Fig. 8, for the elastic case (a) with $dt = 0.8$ ms and the micropolar case (b) with $dt = 0.003$ ms. In both cases the eigenvalues lie in the stable domain, but the latter case requires a much smaller time step. The phase velocities obtained from the eigenvalues are $v_P = \sqrt{E/\rho} = 6.387$ km/s, $v_S = \sqrt{\mu/\rho} = 2.608$ km/s and $v_{R_2} = 1065$ km/s, corresponding to the P, S and R_2 waves, respectively. The latter velocity can also be obtained from Fig. 1 for the wavenumber $k = \sqrt{2}\pi/dx = 0.44$/m. Figure 9 shows snapshots at 210 ms of v_x (a), v_y (b) and η (c), where only the P and S waves can be seen. A small part of the energy as S wave is present in the rotation field η. However, if we compare the particle velocity fields with those of classical elasticity ($\alpha = \gamma = \epsilon = 0$), there is no practical difference, indicating that micro-rotation waves have no effect at low frequencies.

Next, we consider $f_p = 2$ MHz and a grid spacing $dx = dy = 0.1$ mm. The stability analysis indicates that

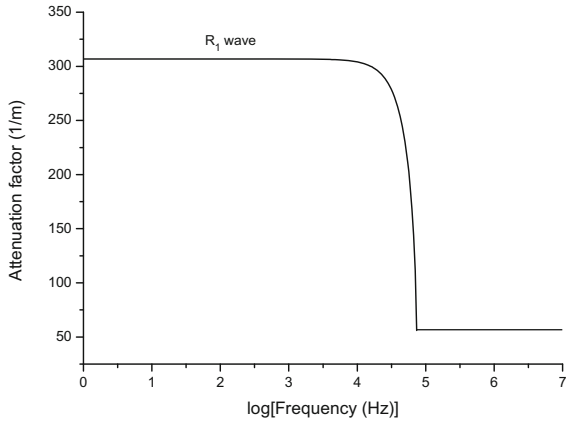


Figure 6
Attenuation factor (46) as a function frequency of the R_1 wave

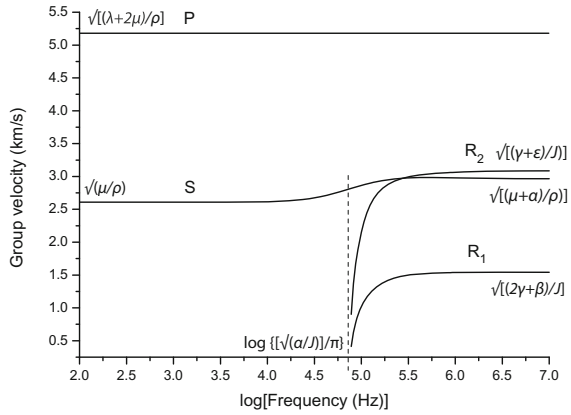


Figure 7
Group velocities of the four wave modes as a function of frequency. The micro-rotation waves exist beyond a cutoff frequency $\omega_0 = 2\sqrt{\alpha/J}$

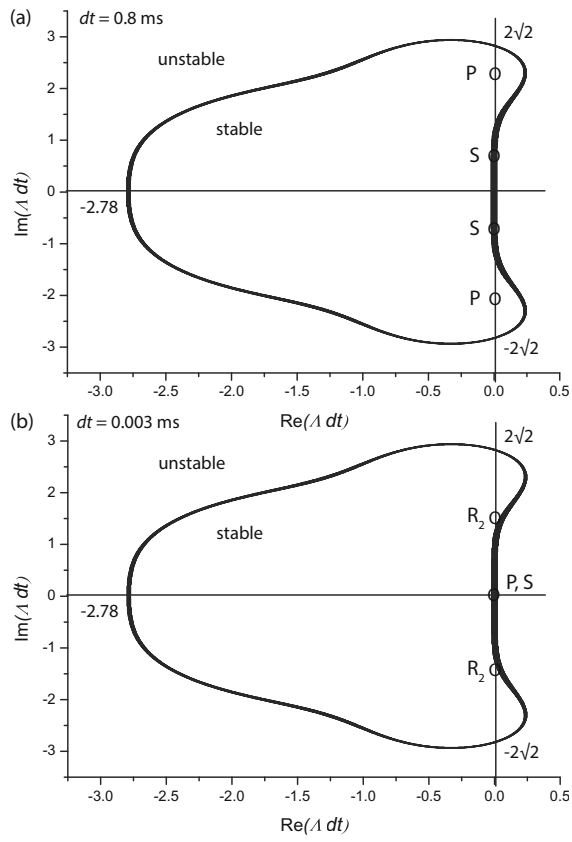
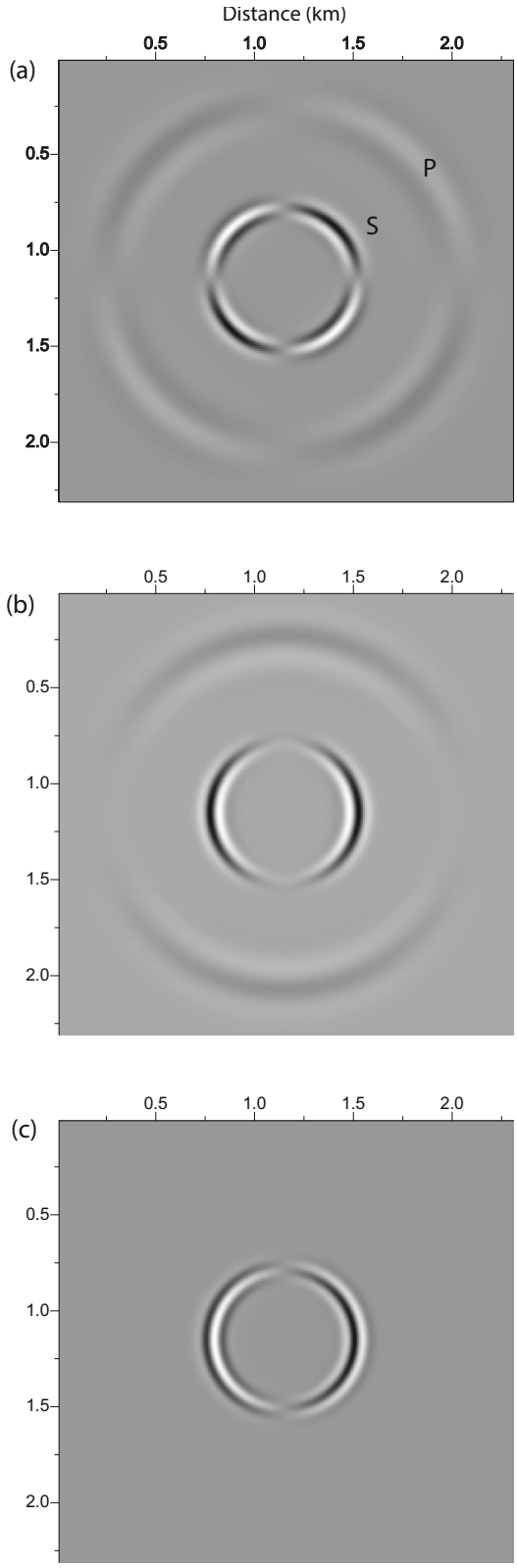


Figure 8
Eigenvalues (times dt) of the propagation matrix in the elastic (**a**) and micropolar (**b**) cases, corresponding to the first system of Eq. (55) at low frequencies. The curve shows the domain of stability of the 4th-order Runge–Kutta algorithm



◀Figure 9
Snapshots at 210 ms of v_x (**a**), v_y (**b**) and η (**c**). The maximum amplitude ratio is 0.52 (a)/1 (b)/0.031 (c). Explicitly, the plots show the P and S waves in the components of the particle velocity, and the S wave in the rate of micro-rotation

dt = 0.008 μs gives eigenvalues (times dt) inside the stable domain (see Fig. 10). The phase velocities obtained from the eigenvalues are $v_{\rm P} = \sqrt{E/\rho}$ = 6.387 km/s, $v_{\rm R_2} = \sqrt{(\gamma+\epsilon)/J}$ =3.085 km/s and $v_{\rm S} = \sqrt{(\mu+\alpha)/\rho}$ = 2.966 km/s, corresponding to the P, R_2 and S waves, respectively, in agreement with the limit velocities of Fig. 1c.

Figure 11 shows snapshots at 1.8 μs of v_x (a), v_y (b), and η (c), where the P and S waves are visible. Contrary to the low-frequency case, the energy is mainly present in the rotation field η. As can be seen in Fig. 10, the velocities of the S and R_2 waves are similar, making it difficult to distinguish the two wavefronts.

Next, we consider the second system of equations and compute the eigenvalues of matrix (56) (times dt) for $dx = dy$ = 0.1 mm and dt = 0.008 μs (see Fig. 12). The phase velocities obtained from the eigenvalues are $v_{\rm R_1} = \sqrt{(2\gamma+\beta)/J}$ = 1.542 km/s, $v_{\rm R_2} = \sqrt{(\gamma+\epsilon)/J}$ =3.085 km/s and $v_{\rm S} = \sqrt{(\mu+\alpha)/\rho}$ = 2.966 km/s, corresponding to the R_1, R_2 and S waves, respectively, in agreement with the limit velocities of Figs. 1c and 5a. We consider f_p = 2 MHz, a grid spacing $dx = dy$ = 0.1 mm and sources in the micro-rotation fields: $Y_1 = Y_2$ = 1. Figure 13 shows snapshots at 4 μs of v_z (a), η_1 (b), and η_2 (c), where the S, R_1 and R_2 waves are visible, The energy is mainly present in the rotational fields.

Nowacki (1974, Eq. 2.13a) set $\boldsymbol{\varphi} = \text{grad}\, \boldsymbol{\Gamma} + \text{curl}\, \mathbf{H}$, and shows that $\boldsymbol{\Gamma}$ and $\mathbf{H}$ satisfy two wave equations representing longitudinal and transverse micro-rotation waves, respectively (Nowacki, 1974, Eq. 2.14). The first vector has non-zero divergence and the second vector has non-zero curl. To verify the polarizations of the micro-rotation waves, we compute the divergence and curl of the vector $\boldsymbol{\eta} = \dot{\boldsymbol{\varphi}}$ (see Eq. (11)), i.e. $\nabla \cdot \boldsymbol{\eta} = \partial_1\eta_1 + \partial_2\eta_2$ and $\nabla \times \boldsymbol{\eta} = \partial_1\eta_2 - \partial_2\eta_1$, respectively, Fig. 14 verifies that R_1 and R_2 have longitudinal and shear

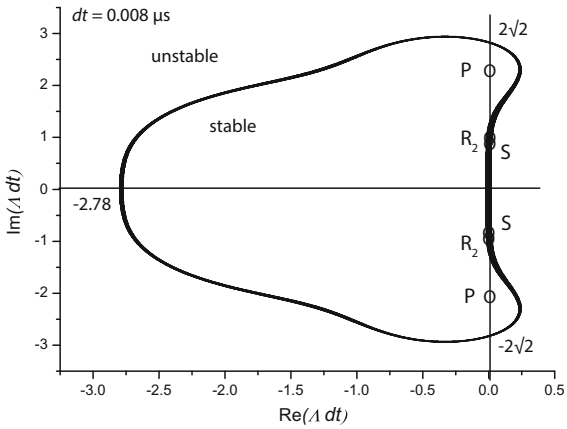


Figure 10
Eigenvalues (times dt) of the propagation matrix, corresponding to the first system of Eq. (55) in the ultrasonic case. The curve shows the domain of stability of the 4th-order Runge–Kutta algorithm

polarizations, respectively. Here, the sources are $T_{12} = T_{21} = 1$.

Let us check whether the energy travels with the group velocity. According to Figs. 4 and 5b, the group velocities of the R_2 and R_1 modes are 2.16 km/s and 1.014 km/s at a frequency of 0.1 MHz, respectively (3.08 km/s and 1.54 km/s at 2 MHz). We consider f_p = 0.1 MHz, a grid spacing of $dx = dy$ = 1 mm, and sources in the micro-rotation fields: $T_{12} = T_{21} = 1$. Figure 15 shows a snapshot at 53 μs of η_2, which indicates that the waves travel at the group velocity predicted by Figs. 4 and 5b, since 53 μs is the time that the R_2 wave employs to travel to the border of the mesh.

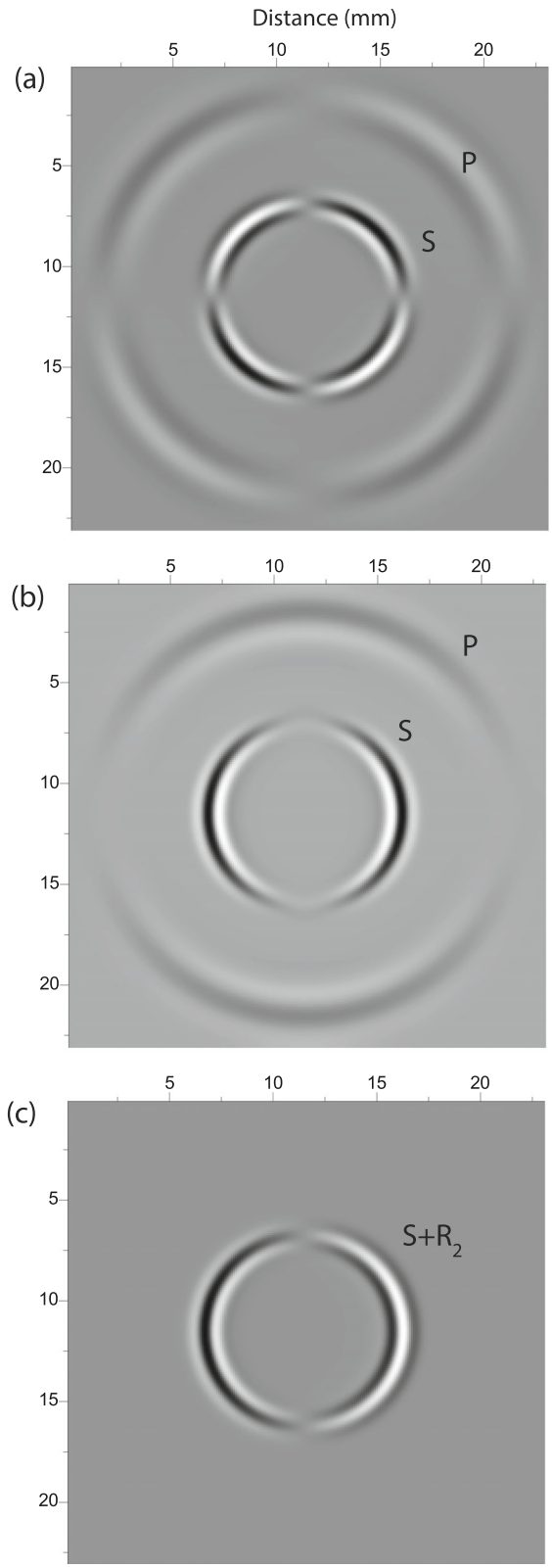
Next we consider an interface separating two media to illustrate how the algorithm can compute wavefields in heterogeneous media. Figure 16 shows a snapshot at 4 μs of v_z (a) and η_1 (b), solution of Eq. (12), where f_p = 2 MHz, $dx = dy$ = 0.1 mm and sources are $T_{12} = T_{21} = 1$. The upper and lower medium have ϵ = 153 kN and 51 kN, respectively. The group velocities of the R_2 waves at 2 MHz are $v_{R_2} = \sqrt{(\gamma + \epsilon)/J}$ =3.080 km/s (upper medium) and 1.951 km/s (lower medium) and this velocity difference can be seen in the location of the R_2 wavefronts. On the other hand, the group velocity of the R_1 wave is 1.542 km/s.

6. Discussion

In the example presented here, micro-rotation waves are a high-frequency phenomenon, and there is a cutoff frequency below which there is no energy associated with these waves. This contrasts with the slow waves in Biot (poroelastic media), which at low frequency exhibit diffusive behavior and allow conversion from fast P wave to slow wave (e.g., Carcione, 2022, Sections 7.16 and 7.26). In the present case, the value of the cutoff frequency determines the existence of micro-rotation waves at low frequencies and their possible applications in Earth sciences. Abreu and co-workers studied this possibility (e.g., Abreu et al., 2017; Abreu, 2025), and particularly Abreu and Duran (2022) presented an alternative micropolar theory that, based on the same physical concepts as the original model, circumvents the problem of the cutoff frequency.

At laboratory frequencies, an experimental study by Merkel et al. (2011) observed coupled rotational-transverse modes in a non-cohesive granular phononic crystal composed of 2 mm stainless steel beads. They measured a cutoff frequency for the rotational-transverse mode between 105 and 170 kHz. This is close to our theoretical 75 kHz cutoff frequency for the R2 wave, and our characteristic length of 2.24 mm matches their physical grain size. Our numerical grid method could be explicitly calibrated to compare the experimental data from these experiments to our simulations, a task that can be reported in a future paper. However, in the experiment by Merkel et al., the rotational-transverse modes were physically triggered using an ultrasonic shear piezo-transducer that applied actual mechanical shear and traction to the boundary of the granular crystal. In this case, applying a point source is not realistic and requires an extended source involving many grid points at the surface of the specimen to simulate a real transducer source, as in Carcione (1998).

Below the cutoff frequency (ω_0), micro-rotation waves are forbidden because our Cosserat model is perfectly elastic and lacks any frictional dissipation. This type of attenuation creates what is known as an "evanescent bandgap" – a frequency range where the wavenumber becomes complex and the wave's



◀Figure 11
Snapshots at 1.8 μs of v_x (**a**), v_y (**b**) and η (**c**), solution of Eq. (10). The maximum amplitude ratio is 0.02 (a)/0.04 (b)/1 (c). Explicitly, the plots show the P and S waves in the components of the particle velocity, and a superposition of the S and R_2 waves in the rate of micro-rotation

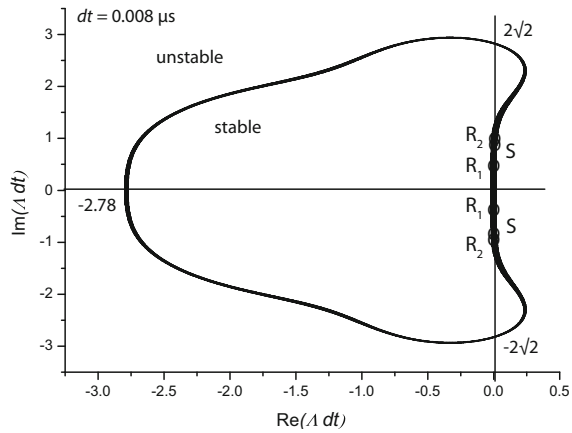
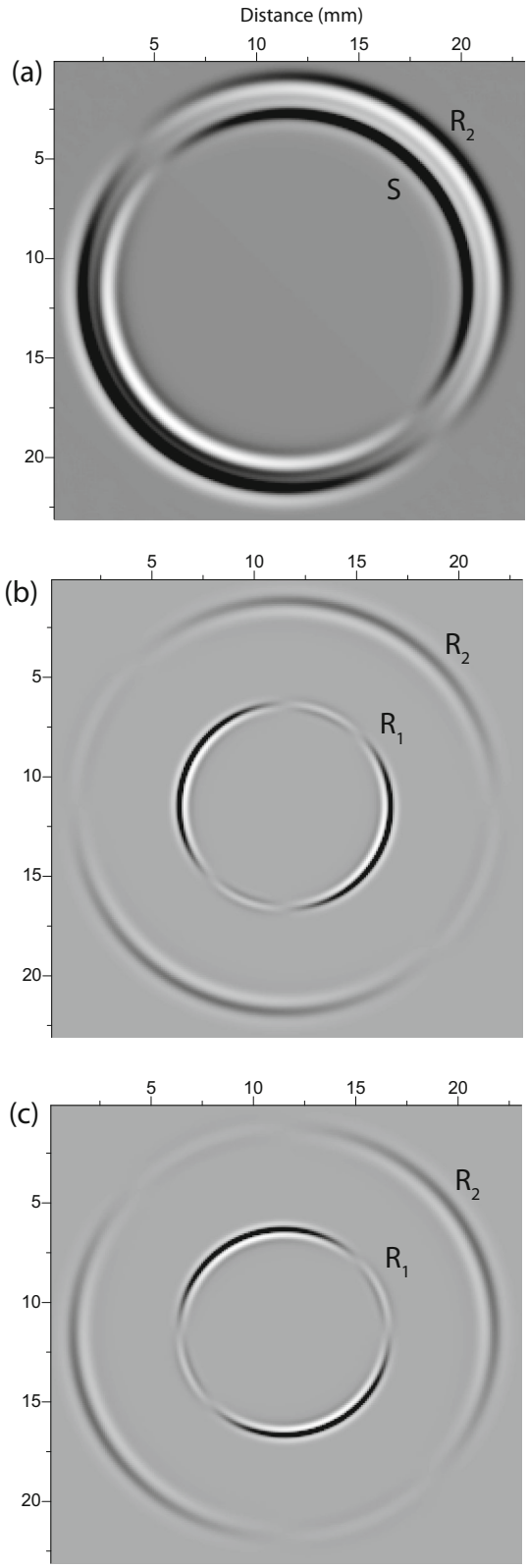


Figure 12
Eigenvalues (times dt) of the propagation matrix, corresponding to the second system of Eq. (56) in the ultrasonic case. The curve shows the domain of stability of the 4th-order Runge–Kutta algorithm

amplitude decays exponentially with distance, rather than losing energy to heat. Essentially, the rotational inertia and stiffness of the microscopic grains act as a mechanical filter, structurally blocking low-frequency rotational waves from propagating through the medium. Abreu (2025) discusses how this specific bandgap might be exploited in practical engineering applications, such as designing acoustic metamaterials (Madeo et al., 2015). He shows how the theory and its extension can be reconciled in a single equation, with direct and documented applications in areas such as civil engineering (Timoshenko's equation), solid-state physics (lattice theory), seismic metamaterials (materials with frequency band gaps), granular materials (micropolar model), and biological materials (microstretch model).



◀Figure 13
Snapshots at 4 μs of v_z (**a**), η_1 (**b**) and η_2 (**c**), solution of Eq. (12), where f_p = 2 MHz, $dx = dy$ = 0.1 mm and sources in the micro-rotation fields: $Y_1 = Y_2 = 1$. Explicitly, the plots show the particle velocity (a), and the two micro-rotation components (b and c). The maximum amplitude ratio is 0.00023 (a)/1 (b)/1 (c). The phase velocities of the S, R_1 and R_2 waves are $v_S = \sqrt{(\mu+\alpha)/\rho} = 2.966$ km/s, $v_{R_1} = \sqrt{(2\gamma+\beta)/J} = 1.542$ km/s, and $v_{R_2} = \sqrt{(\gamma+\epsilon)/J} = 3.085$ km/s, respectively

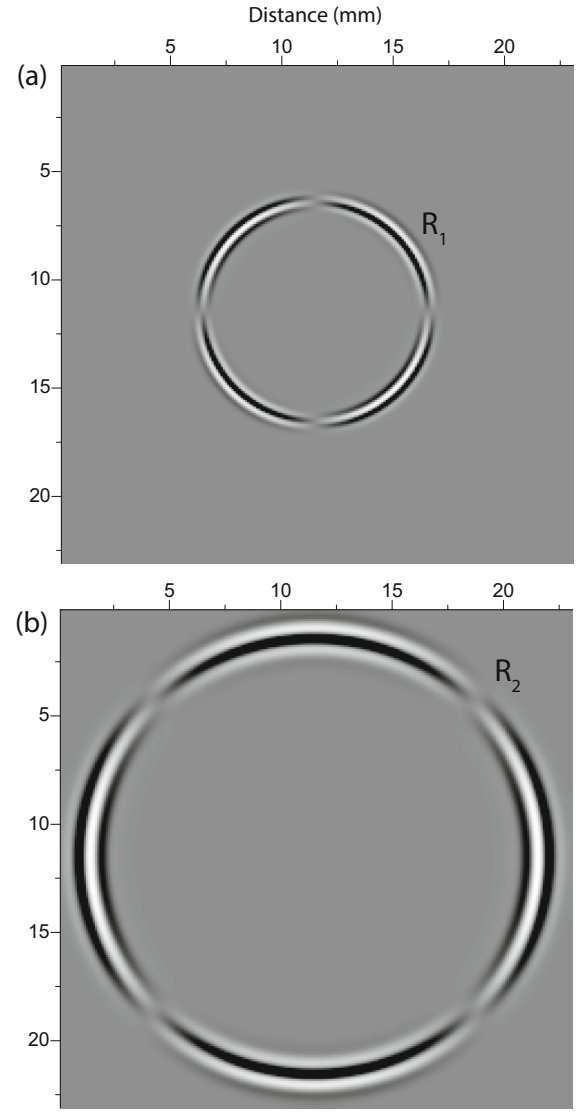


Figure 14
Snapshots at 4 μs of $\nabla \cdot \boldsymbol{\eta}$ (**a**) $\nabla \times \boldsymbol{\eta}$ (**b**), showing that R_1 and R_2 have longitudinal and shear polarizations, respectively

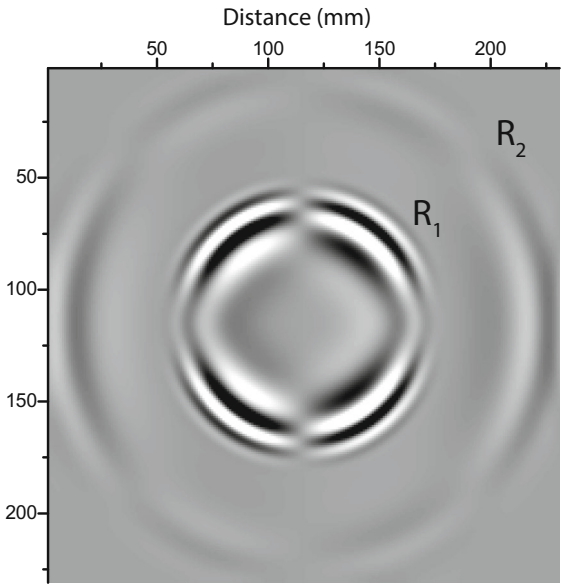


Figure 15
Snapshot at 53 μs of η_2, where f_p = 0.1 MHz, $dx = dy$ = 1 mm and sources are $T_{12} = T_{21}$ = 1

7. Conclusions

We have numerically solved the differential equations for wave propagation based on the Cosserat micropolar theory. This theory shares the same foundation as classical elasticity but explicitly accounts for micro-rotations of the material particles (e.g. grains), resulting in asymmetric stress and strain tensors. The plane-wave theory predicts the classical P and S waves, as well as two micro-rotation waves one with longitudinal polarization (R_1) and the other with transverse polarization (R_2). These predictions are confirmed by the stability analysis and full-wave simulations, which are based on the 4th-order Runge–Kutta algorithm for time stepping and the Fourier pseudospectral method to compute the spatial derivatives.

It is found that, in the example presented here, micro-rotation waves are a high-frequency phenomenon. The distinction between low and high frequencies is determined by a cutoff frequency, which in this example is 75 kHz. However, in geological and/or inhomogeneous media, a different cutoff frequency and mode conversion could have practical implications, for instance, in overpressured sandstones or unconsolidated rocks, where the grains are partially or not cemented.

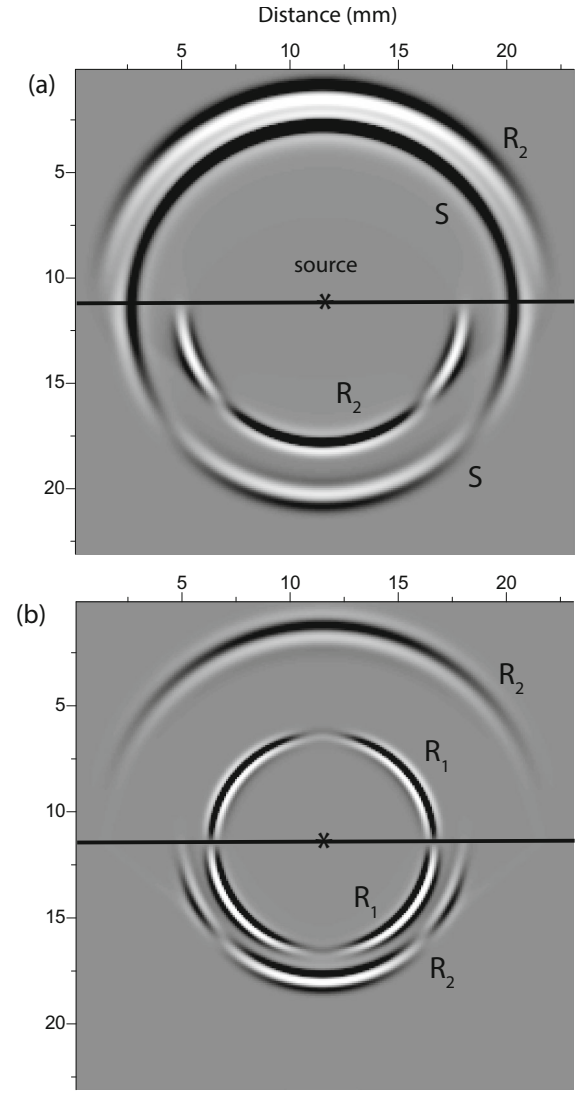


Figure 16
Snapshot at 4 μs of v_z (**a**) and η_1 (**b**), solution of Eq. (12), where f_p = 2 MHz, $dx = dy$ = 0.1 mm and sources are $T_{12} = T_{21}$ = 1. The upper and lower medium have ϵ = 153 kN and 51 kN, respectively

Acknowledgements

We thank an anonymous reviewer for their precise and detailed suggestions, and for proposing an additional statement to clarify the physics of the micro-rotation waves.

Author Contributions J.B., J. M. C., and M.A. wrote the main manuscript text, and J. B., A. N. Q. and J. E.S. prepared the figures. All authors reviewed the manuscript.

Funding

This work was supported by the National Science and Technology Major Project of the Ministry of Science and Technology of China (No.2025ZD1402704-03).

Data Availability

The authors confirm that there is no data supporting the findings of this study.

Declarations

Conflict of interest There are no conflicts to report and/or disclose.

Ethics approval There is no ethical approval to declare.

A Stability Analysis

Let us consider the plane wave

$$\mathbf{v} = \mathbf{v}_0 \exp[\mathrm{i}(\omega_c t - k_1 x - k_2 y)] \tag{54}$$

where ω_c is the complex frequency, solution of Eq. (49), which gives an eigenvalue equation for the eigenvalues $\Lambda = \mathrm{i}\omega_c$: $\det(\mathbf{M} - \Lambda \mathbf{I}_9) = 0$, where

$$\mathbf{M} = \begin{pmatrix} 0 & 0 & 0 & -\mathrm{i}k_1\rho' & 0 & 0 & -\mathrm{i}k_2\rho' & 0 & 0 \\ 0 & 0 & 0 & 0 & -\mathrm{i}k_2\rho' & -\mathrm{i}k_1\rho' & 0 & 0 & 0 \\ 0 & 0 & 0 & 0 & 0 & J' & -J' & -\mathrm{i}k_1 J' & -\mathrm{i}k_2 J' \\ -\mathrm{i}k_1 E & -\mathrm{i}k_2\lambda & 0 & 0 & 0 & 0 & 0 & 0 & 0 \\ -\mathrm{i}k_1\lambda & -\mathrm{i}k_2 E & 0 & 0 & 0 & 0 & 0 & 0 & 0 \\ -\mathrm{i}k_2(\mu-\alpha) & -\mathrm{i}k_1(\mu+\alpha) & -2\alpha & 0 & 0 & 0 & 0 & 0 & 0 \\ -\mathrm{i}k_2(\mu+\alpha) & -\mathrm{i}k_1(\mu-\alpha) & +2\alpha & 0 & 0 & 0 & 0 & 0 & 0 \\ 0 & 0 & -\mathrm{i}k_1(\gamma+\epsilon) & 0 & 0 & 0 & 0 & 0 & 0 \\ 0 & 0 & -\mathrm{i}k_2(\gamma+\epsilon) & 0 & 0 & 0 & 0 & 0 & 0 \end{pmatrix}, \tag{55}$$

and $\mathbf{I}_9$ is the 9×9 identity matrix.

Let us now consider the second system of Eq. (51). Matrix $\mathbf{M}$ is

$$\mathbf{M} = \begin{pmatrix} 0 & 0 & 0 & -\mathrm{i}k_1\rho' & 0 & -\mathrm{i}k_2\rho' & 0 & 0 & 0 & 0 & 0 \\ 0 & 0 & 0 & 0 & 0 & J' & -J' & -\mathrm{i}k_1 J' & 0 & 0 & -\mathrm{i}k_2 J' \\ 0 & 0 & 0 & -J' & J' & 0 & 0 & 0 & -\mathrm{i}k_2 J' & -\mathrm{i}k_1 J' & 0 \\ -\mathrm{i}k_1(\mu+\alpha) & 0 & 2\alpha & 0 & 0 & 0 & 0 & 0 & 0 & 0 & 0 \\ -\mathrm{i}k_1(\mu-\alpha) & 0 & -2\alpha & 0 & 0 & 0 & 0 & 0 & 0 & 0 & 0 \\ -\mathrm{i}k_2(\mu+\alpha) & -2\alpha & 0 & 0 & 0 & 0 & 0 & 0 & 0 & 0 & 0 \\ -\mathrm{i}k_2(\mu-\alpha) & 2\alpha & 0 & 0 & 0 & 0 & 0 & 0 & 0 & 0 & 0 \\ 0 & -\mathrm{i}k_1(2\gamma+\beta) & -\mathrm{i}k_2\beta & 0 & 0 & 0 & 0 & 0 & 0 & 0 & 0 \\ 0 & -\mathrm{i}k_1\beta & -\mathrm{i}k_2(2\gamma+\beta) & 0 & 0 & 0 & 0 & 0 & 0 & 0 & 0 \\ 0 & -\mathrm{i}k_2(\gamma-\epsilon) & -\mathrm{i}k_1(\gamma+\epsilon) & 0 & 0 & 0 & 0 & 0 & 0 & 0 & 0 \\ 0 & -\mathrm{i}k_2(\gamma+\epsilon) & -\mathrm{i}k_1(\gamma-\epsilon) & 0 & 0 & 0 & 0 & 0 & 0 & 0 & 0 \end{pmatrix}. \tag{56}$$

When using the Fourier pseudospectral method for computing the spatial derivatives, the wavenumbers supported by the numerical mesh span from $k_1 = 0$ and $k_2 = 0$ to the Nyquist wavenumbers $k_1 = \pi/dx$ and $k_2 = \pi/dy$, where dx and dy are the grid spacings. According to Jain (1984, p. 71-72, Fig. 2.7) all complex eigenvalues must lie with the domain of stability of the Runge–Kutta algorithm. For a real eigenvalue, $-2.78 < dt\Lambda < 0$, and for an imaginary eigenvalue $0 < |dt\Lambda| < 2\sqrt{2}$, where dt is the time step. The eigenvalues in the elastic case ($\alpha = \gamma = \epsilon = 0$) lie in the imaginary Λ axis and $\mathrm{Im}(\Lambda)/k$, where $k = \sqrt{k_1^2 + k_2^2}$ gives the phase velocity. The eigenvalues of matrix **M** are obtained with subroutine CG from the eigen-system package (eispack) to find the eigenvalues and eigenvectors of a complex general matrix (https://www.netlib.org/eispack/).

Publisher's Note Springer Nature remains neutral with regard to jurisdictional claims in published maps and institutional affiliations.

Springer Nature or its licensor (e.g. a society or other partner) holds exclusive rights to this article under a publishing agreement with the author(s) or other rightsholder(s); author self-archiving of the accepted manuscript version of this article is solely governed by the terms of such publishing agreement and applicable law.

References

Abreu, R. (2025). Micropolar modeling of shear wave dispersion in marine sediments and deep Earth materials: Deriving scaling laws. *Geosciences, 15*, 124.

Abreu, R., & Duran, S. (2022). Understanding micropolar theory in the Earth sciences I: The eigenfrequency ω_r. *Pure and Applied Geophysics, 179*, 915–932.

Abreu, R., Kamm, J., & Reiß, A.-S. (2017). 2017, Micropolar modelling of rotational waves in seismology. *Geophysical Journal International, 210*, 1021–1046.

Buklakov, E. A., Roux, J. N., & Grekova, E. F. (2023). Simulation of wave propagation in weakly cohesive powders by discrete element method, 2023 Days on Diffraction (DD), St.Petersburg. *Russian Federation, 2023*, 19–24.

Carcione, J. M., Gei, D., Fu, L.-Y., & Ba, J. (2025). Wave simulation in 2D anisotropic media with asymmetric stress and strain tensors submitted to Wave Motion.

Carcione, J. M. (1998). Scattering of elastic waves by a plane crack of finite width in a transversely isotropic medium. *International Journal of Numerical and Analytical Methods in Geomechanics, 22*, 263–275.

Carcione, J. M. (2022). Wave fields in real media. Theory and numerical simulation of wave propagation in anisotropic, anelastic, porous and electromagnetic media. Elsevier. 4th edition.

Cosserat, E., & Cosserat, F. (1909). *Theorie des corps deformables*. Paris: A. Hermann et fils.

Dębski, W. (2025). Rotational waves in amorphic media discrete element method simulations, Presentation at the 7th IWGoRS meeting. *Opole, Poland*. https://doi.org/10.13140/RG.2.2.35838.29765

Dhabu, A. C., Singla, V. K., & Raghukanth, S. (2021). Seismic wave propagation through layered reduced micropolar medium. *Journal of Geophysical Research: Solid Earth, 126*, e2020JB020931.

Hadjesfandiari, A. R., & Dargush, G. F. (2011). Couple stress theory for polar solids. *International Journal of Solids and Structures, 48*(18), 2496–2510.

Hassanpour, S., & Heppler, G. R. (2014). Step-by-step simplification of the micropolar elasticity theory to the couple-stress and classical elasticity theories. *IMECE2014*, (p. 1–9).

Hassanpour, S., & Heppler, G. R. (2015). Micropolar elasticity theory: A survey of linear isotropic equations, representative notations, and experimental investigations. *Mathematics and Mechanics of Solids*, I-19.

Jain, M. K. (1984). Numerical solution of partial differential equations. New Delhi. 2nd edition.

Lakes, R. S. (1986). Experimental microelasticity of two porous solids. *International Journal of Solids and Structures, 22*(1), 55–63.

Madeo, A., Neff, P., Ghiba, I. D., Placidi, L., & Rosi, G. (2015). 2015, Wave propagation in relaxed micromorphic continua: Modeling metamaterials with frequency band-gaps. *Continuum Mechanics and Thermodynamics, 27*, 551–570.

Merkel, A., & Luding, S. (2017). Enhanced micropolar model for wave propagation in ordered granular materials. *International Journal of Solids and Structures, 106–107*, 91–105.

Merkel, A., Tournat, V., & Gusev, V. (2011). Experimental evidence of rotational elastic waves in granular phononic crystals. *Physical Review Letters, 107*, Article 225502.

Nowacki, W. (1974). *Micropolar elasticity, Courses and Lectures 151 (Udine, 1972)*. Springer-Verlag.

Nowacki, W., & Nowacki, W. K. (1969). Generation of waves in an infinite micropolar elastic solid body I. *Bulletin de l'Academie Polonaise des Sciences, XVII, 2*, 75–82.

Parfitt, V. R., & Eringen, A. C. (1966). Reflection of plane waves from the flat boundary of a micropolar half-space, General Technology Corporation. *Technical Report* 8–3.

Pujol, J. (2009). Tutorial on rotations in the theories of finite deformation and micropolar (Cosserat) elasticity. *Bulletin of the Seismological Society of America, 99*(2B), 1011–1027.

Qiu, Z. (2020). A simple theory of asymmetric linear elasticity. *World Journal of Mechanics, 10*, 166–185.

Sadovskaya, O., & Sadovskii, V. (2012). *Mathematical modeling in mechanics of granular materials*. Springer-Verlag.

Sluys, L. J. (1992). Wave propagation, localisation, and dispersion in softening solids. Delft University. Ph.D. Thesis.

Xiu, C., Chu, X., Wan, J., & Wang, J. (2020). Numerical simulation of impulse waves in Cosserat media based on a time-discontinuous Galerkin finite element method. *International Journal for Numerical Methods in Engineering, 122*(17), 4507–4540.

(Received January 20, 2026, revised April 14, 2026, accepted May 11, 2026, Published online June 19, 2026)